Chapter 3

Experimental techniques

The atomic structure and chemical composition of the surface region are two of the most fundamental areas of interest in surface science. The Warwick modular CAICISS system is equipped with several tools for investigating these properties. This chapter introduces the system itself and the theoretical aspects of ion scattering techniques in general and CAICISS in particular. In addition, some brief discussion of LEED and XPS is also included.

3.1 The Warwick CAICISS system

The CAICISS technique was originally developed by Mazakazu Aono and co-workers at the RIKEN Laboratory in Tokyo in the late 1980's [80]. CAICISS is a modification of LEIS, utilising a near-180° total scattering angle in order to simplify the analysis of the ion scattering process as the shadowing and blocking effects can be easily deconvoloved (i.e. an atom that can penetrate into the near-surface region can also reach the detector after a 180° scattering event). Indeed, the near-180° scattering geometry employed in CAICISS means that the trajectories of the detected ions and neutral particles are dominated by blocking effects after the scattering event. A move away from electrostatic analysers was also introduced leading to the introduction of channel plate detectors. This meant that both scattered ions and neutral particles could be detected in time-of-flight (ToF) mode, allowing information from the near-surface region to be recorded. However, the ToF measurements coupled with the coaxial geometry necessitates the pulsing of the incident ion beam, therefore decreasing the overall ion flux and the implementation of more complicated electronics to generate the ion pulses. This reduction in ion flux can be partially overcome when uncharged scattered particles are also detected and a detector with a high efficiency is employed. The basis of the technique does put a considerable constraint on the arrangement of

the ion source, beamline and detector, but only one port on the scattering chamber is utilised by the CAICISS technique, therefore meaning that CAICISS can be considered to be a *bolt-on* technique. As long as there is clear line-of-sight to the sample, CAICISS can be used as a dynamic technique to monitor the growth of thin films in real time [81].

The modular CAICISS system used for the investigations detailed in this thesis was based on the same design concept as Aono's original design, and was constructed at Warwick [81]. Various sections of the system are shown in figures 3.1, 3.2, 3.3 and 3.4 [5, 81, 82].

The Nielson ion source [83] used on the Warwick system is capable of producing ion beams with high current density, low energy spread and possess a highly efficient ionisation process which results in a very low proportion of neutral particles in the final beam. In addition, Nielson sources consume less power than comparable ion sources. With reference to the schematic shown in figure 3.1, a current of around 15 A is passed through the Ta filament within the source, producing electrons by thermionic emission. To increase the probability of the electrons ionising a noble gas atom, the

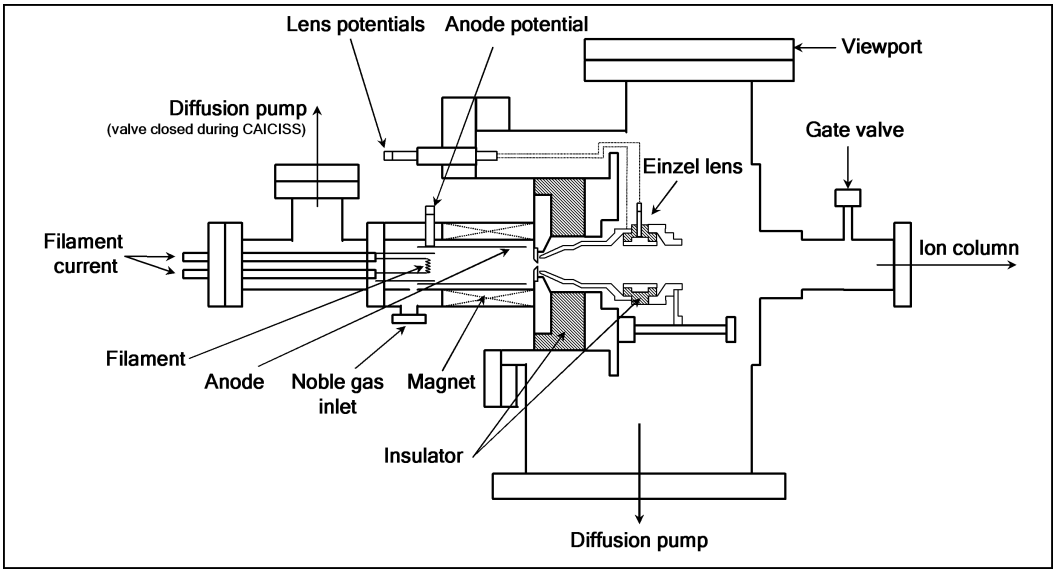

Figure 3.1: Schematic diagram of the Nielson ion source. The makeup and operation of the source is described in the main text.

path length of the electron is increased by the production of perpendicular electric and magnetic fields. This causes the electron paths to spiral. The filament is held at the same potential as the anticathode, with the anode held at a potential $\sim$ 100 V higher. This confines the plasma and provides a potential difference which drives the discharge from the filament. An extraction potential, negative with respect to the anode, is applied to the first two elements of the einzel lens, providing some initial focussing of the beam. This entire section of the source is floated to the desired ion beam potential. The final lens is earthed and therefore provides the high positive potential which defines the energy of the emitted ions. Further details of the design and commissioning of the ion source are given elsewhere [81].

The CAICISS ion source is capable of producing either He^+ or Ne^+ monoenergetic ion beams in a 0.75 - 3.4 keV energy range. Following extraction from the source, the ions are electrostatically steered along the ion column to a sample residing in the main chamber. The beam steering section of the ion column, shown in figure 3.2, consists of one vertical pair and two horizontal pairs of beam steering plates, as well as a pair

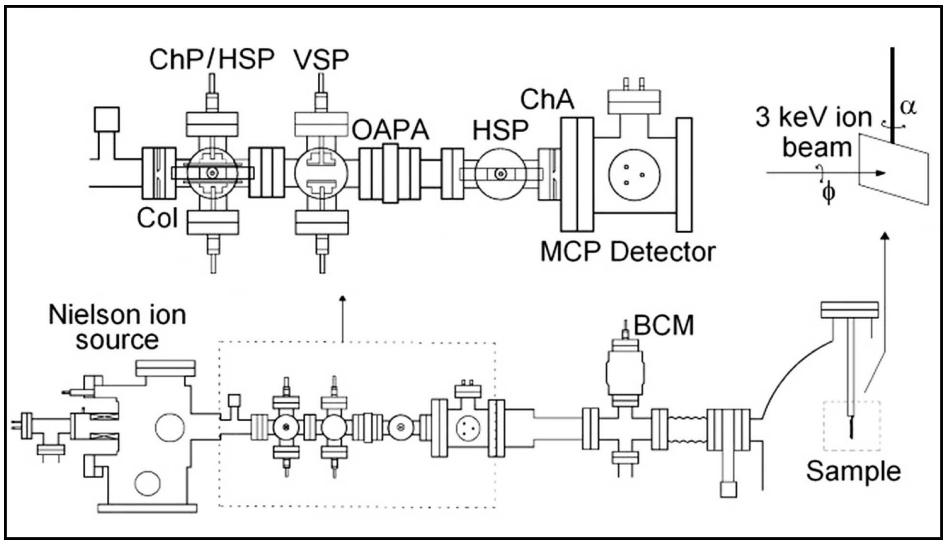

Figure 3.2: Schematic diagram of the Warwick CAICISS apparatus. Several components are labelled in the central section of the ion column (upper image): MCP, microchannel plate detector; OAPA, off-axis port aligner; ChP, chopping plates; ChA, chopping aperture; BCM, beam current monitor; HSP and VSP, horizontal and vertical steering plates; Col, collimating aperture. The axes defining the polar angle, α, and azimuthal angle, ϕ, are shown in the upper-right quadrant.

of vertical chopping plates, and includes a 2° bend (the off-axis port aligner) to filter out any neutral particles produced by the source. The plates are used to direct the beam in such a manner that short ($\sim$ 60 ns) pulses of ions pass through the final aperture in the steering section. The ions then travel through an 8 mm diameter hole in the center of the detector and on to the surface of the sample located in the main chamber (figures 3.3 and 3.4). The ions are then scattered through 179° $\pm$ 1°, travel back along the ion column and strike the microchannel plate (MCP) detector, capable of detecting ions and neutral particles, mounted coaxially with the ion beam at a distance of 0.8 m from the sample. As the incident ions are pulsed with a frequency of approximately 10 kHz, the backscattered yield from the surface can be measured in time-of-flight (ToF) mode, using an EG&G Ortec MCB and Maestro II software. The ToF can then be used to calculate the energies of the scattered particles and hence the atomic masses of the atoms in the surface region. For polar angle scans, the rotation of the sample has been automated using a stepper motor. The motor is controlled by the data acquisition computer and rotates the sample by 1.8° at the completion of each step of the experiment. At the completion of the experiment, the individual intensity vs. ToF spectra are collated on a single three-dimensional plot showing the backscattered intensity as a function of both the flight time and the polar angle. The steps required in the analysis of the 3D plot will be discussed in chapter 4.

An MCP is essentially an array of electron multipliers [84, 85]. The channels are 20 μm in diameter, giving a channel density of $\sim$ 3000 channels per mm^2, and are 2 mm in length. The channels are made of glass, with an internal coating of a high secondary electron emitting material. When an ion (or neutral particle) collides with the surface, an electron cascade is initiated leading to an amplification of the signal by a factor of $\sim 10^3$. Tobita and co-workers have shown that such microchannel plates have equal and constant efficiencies for He^+ and He^0 in a 1-10 keV incident energy range [86], making such a detector ideal for a CAICISS system.

The detector on the CAICISS ion column consists of three MCPs connected in series to amplify the detected signal by a factor of up to 10^{10}. The design is such that the electron multiplication paths are minimised to ensure that their contribution

to the time resolution of the system is negligible. The MCPs are mounted on 44 mm diameter discs with an 8 mm diameter hole in the center to allow the passage of the incident ion beam. The dimensions of the MCPs result in the detection of particles backscattered through angles ranging from 178° to 179.8°. The surface of the first MCP is earthed, hence providing a field-free region for the backscattered ions.

To ensure a high-purity ion beam and a contaminant-free column and main chamber, the system is pumped using two diffusion pumps and one ion pump. The main chamber has a base pressure in the region of 2×10^{-10} mbar, and is also equipped with a cold cathode ion gun for IBA (Vacuum Generators, UK), a TC-50 thermal gas cracker for AHC and gas adsorption (Oxford Applied Research, UK), a retractable LEED optic (Omicron GmbH, Germany), an X-ray source and hemispherical analyser for XPS (VSW, UK), a 5 keV electron gun for AES (VSW), and a metal evaporation source for Pt deposition. The arrangement of these components is shown in figures 3.3 and 3.4. All samples investigated were mounted on a manipulator capable of x-y-z

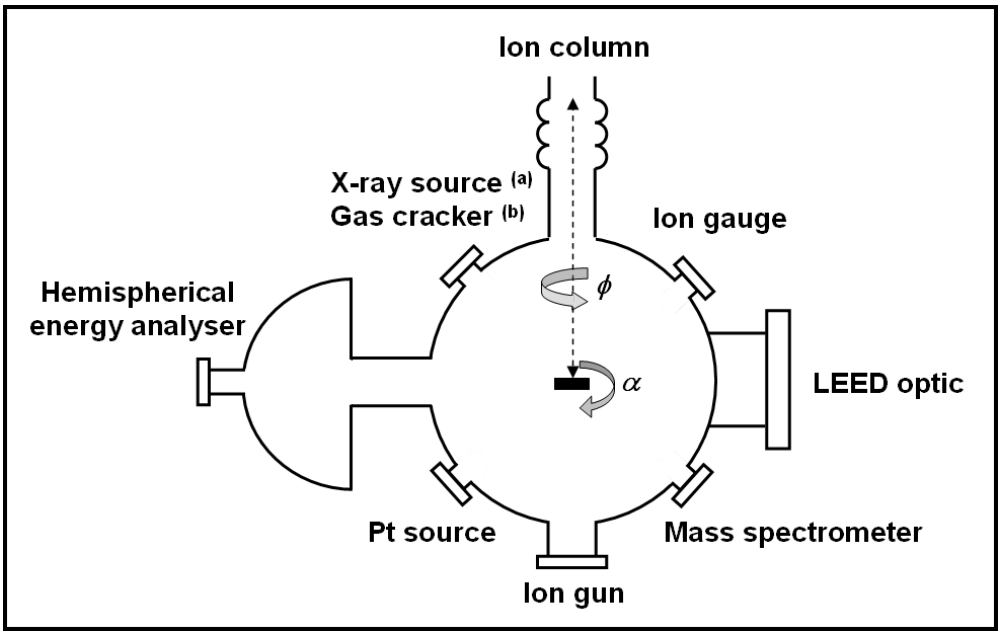

Figure 3.3: Schematic representation of the main chamber of the Warwick CAICISS system with the main components labelled. Where two components are attached to the chamber at the same angle with respect to the sample surface (α), components on the upper level are labelled (a) whilst lower level components are labelled (b).

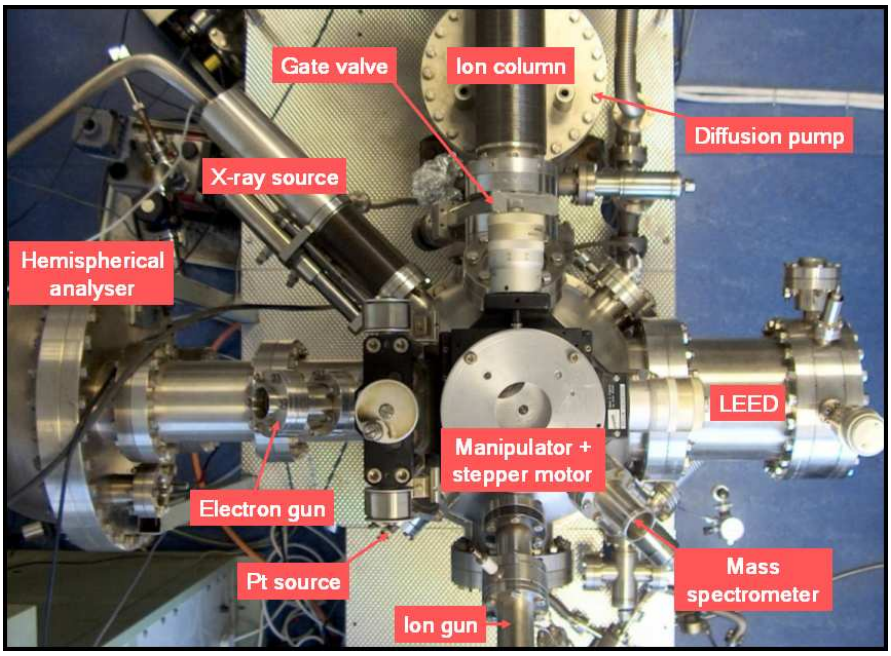

Figure 3.4: A top-down view of the main chamber of the Warwick CAICISS system with main components labelled. The thermal gas cracker resides directly underneath the X-ray source, and therefore is not visible from this angle.

translation in addition to polar (α) and azimuthal (ϕ) rotation with respect to the central axis of the ion column (see figure 3.2). In addition, the manipulator offers the opportunity to heat samples to approximately 800°C via resistive heating, monitored by a chromel-alumel thermocouple in contact with the sample.

3.2 Ion scattering spectroscopy

3.2.1 The basics of ion scattering

In a typical ion scattering experiment, a beam of mono-energetic inert gas ions strikes the surface of a sample at an incident angle, α, with respect to the surface layer of the crystal. In the low energy regime, the majority of the ions will be elastically scattered by the atoms at the surface, with their energy being measured at an angle θ, as demonstrated in figure 3.5. Assuming a kinematic binary collision, and having a knowledge of the incident energy (E_0), primary ion mass (M_1), scattering angle (θ) and the scattered ion energy (E_1), it is possible to calculate the mass of the scattering

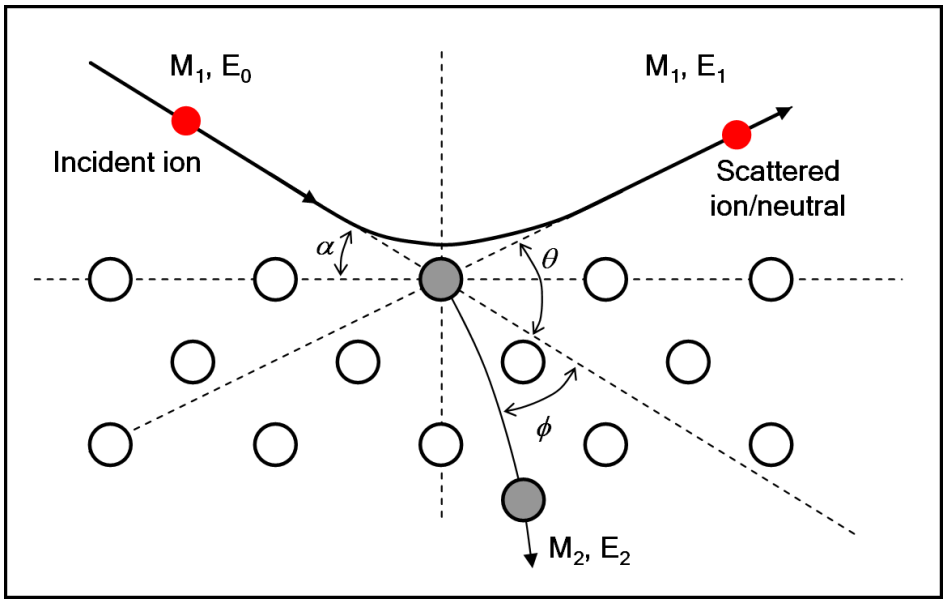

Figure 3.5: Schematic demonstration of an ion scattering from a surface atom. An ion with mass M_1 and kinetic energy E_0 is incident at an angle α on a target atom with mass M_2. The ion is scattered through an angle θ with respect to the incident direction, losing kinetic energy to the target atom during the collision. The scattered ion possesses a kinetic energy E_1, whilst the target atom recoils with a kinetic energy E_2.

atom (M_2) by:

$$\frac{E_1}{E_0} = \frac{1}{(1+A)^2}\left(\cos\theta \pm \sqrt{A^2 - \sin^2\theta}\right)^2 \tag{3.1}$$

where $A = M_2/M_1$, and E_1/E_0 is also known as the *kinematic factor*, k. Ions elastically scattered from atoms with differing mass will possess different kinetic energies and hence different velocities. This allows a scattered ion yield for each element in the surface region to be obtained by detecting the scattered ions and neutrals in time-of-flight (ToF) mode.

Equation 3.1 demonstrates the major advantage of the CAICISS technique, since in such experiments $\theta \simeq 180°$. This condition leads to a simplification of equation 3.1 encompassing the conservation of energy and momentum in this geometry such that:

$$\frac{E_1}{E_0} = k = \frac{(A-1)^2}{(A+1)^2} \tag{3.2}$$

Therefore, knowledge of the time-of-flight corresponding to a feature in the CAICISS

data can be rather simply translated into the scattered particle energy and hence the mass of the scattering atom, M_2, can be determined. Equation 3.2 also shows that for the best mass resolution a heavier incident ion species, such as Ne^+, should be used as this reduces the value of A and hence also reduces k. Using Ne increases the mass resolution approximately by a factor of 4 when compared to He. However, using Ne creates complications in data analysis due to the inability to obtain isotopically pure Ne gas (^{20}Ne:^{22}Ne = 90:10), as well as inducing a larger degree of damage to the surface caused by the larger mass of the incident ions. In this project, atomic species with widely differing masses have been investigated and so all CAICISS experiments were conducted with pure ^{4}He gas (Air Products, UK).

The backscattered intensity, I, is dependent on the scattering cross-section, σ [81, 87]. The differential scattering cross-section, $d\sigma/d\Omega$, is given by:

$$\frac{d\sigma}{d\Omega} = C\frac{(Z_1 Z_2 e^2/4E)^2}{\sin^4(\theta/2)}\left(\frac{1}{4\pi\epsilon_0}\right)^2 \tag{3.3}$$

where C represents a correction factor required due to the screened Coulombic potential present in low energy ion scattering (discussed below). This correction is not required (ie. $C = 1$) for higher incident energies, such as those used in MEIS ($E_0 \sim$ 100 keV) and RBS ($E_0 \sim 1$ MeV). The scattered ion intensity is given by:

$$I = \frac{d\sigma}{d\Omega}\, I_0\, N\, S\, P^+\, T\, \Delta\Omega \tag{3.4}$$

where $\Delta\Omega$ is the acceptance angle of the detector, I_0 the intensity of the incident ion beam, N the number density of the scattering atoms, P^+ the probability of neutralisation of the incident ion, T the transmission coefficient of the analyser (including the efficiency of the detector) and S the structure parameter related to the incident and outgoing trajectories which expresses the probability of an atom being hit by the primary beam. The detected intensity is reduced in CAICISS when compared to other LEIS techniques due to the need to pulse the incident ion beam, therefore reducing I_0. However, P^+ can be set to 1 for CAICISS due to the use of a detector which

measures the time-of-flight of both scattered ions and neutral particles, thus increasing the detected intensity.

3.2.2 Interaction potentials

The 'billiard ball' picture of ion scattering serves as a good introduction to the technique. However, the process is more accurately described by the Coulombic interaction between the incident ion and the target atom. When an ion with nuclear charge Z_1e approaches a surface atom with charge Z_2e, the ion will be scattered due to the Coulomb repulsive interaction between the two particles. This basic interaction is true for short interaction times (and hence high energy ($\sim$ MeV) ions), but at lower energies such as those used in CAICISS we have to consider the effect of electrons screening the positive nucleus of the scattering atom. The most widely used potentials consist of a Coulombic ($1/r$) term and a screening function, $\Phi(r/a)$, as shown in equation 3.5.

$$V(r) = \frac{Z_1 Z_2 e^2}{4\pi\epsilon_0 r}\,\Phi(r/a) \tag{3.5}$$

Two forms of the screening function are widely used in LEIS data analysis [87]. Firstly, the Molière approximation to the Thomas-Fermi model (TFM), where $\Phi(r/a)$ takes the form:

$$\begin{aligned}\Phi(r/a) = 0.35\ exp\left(-0.3\frac{r}{a}\right) + 0.55\ exp\left(-1.2\frac{r}{a}\right) \\ + 0.1\ exp\left(-6.0\frac{r}{a}\right)\end{aligned} \tag{3.6}$$

where the screening length, a (in Å), is given by either the Firsov [88] or Lindhard [89] expressions:

$$a_{Firsov} = \frac{0.4685}{\left(\sqrt{Z_1} + \sqrt{Z_2}\right)^{2/3}} \tag{3.7}$$

$$a_{Lindhard} = \frac{0.4685}{\left(\sqrt{{Z_1}^{2/3} + {Z_2}^{2/3}}\right)} \tag{3.8}$$

In the low energy regime employed in LEIS, these screening lengths are often reduced by the use of a screening constant, *C*, given by the expression [90]:

$$C = 0.54 + 0.045\left(\sqrt{Z_1} + \sqrt{Z_2}\right) \tag{3.9}$$

The applicability of equation 3.9 to CAICISS experiments will be discussed briefly in chapter 8. Alternatively, the universal Ziegler-Biersack-Littmark (ZBL) function can be used, where the screening function can be expressed as:

$$\begin{aligned}\Phi(r/a) = 0.0281\ exp\left(-0.2016\frac{r}{a}\right) + 0.2802\ exp\left(-0.4029\frac{r}{a}\right) \\ + 0.5099\ exp\left(-0.9423\frac{r}{a}\right) + 0.1818\ exp\left(-3.2\frac{r}{a}\right)\end{aligned} \tag{3.10}$$

where the screening length is given by:

$$a_{ZBL} = \frac{0.4685}{\left(Z_1^{0.23} + Z_2^{0.23}\right)^{1/2}} \tag{3.11}$$

Both the theoretical TFM and ZBL interaction potentials give similar results for most LEIS applications [90]. However, due to the inability to model the exact nature of the interaction, the potentials have to be modified slightly to gain a more accurate agreement on an experiment-by-experiment basis. Once the potential has been modelled, it can be used to obtain quantitative information on the surface structure by studying the shape of the shadow cones.

3.2.3 Shadowing and blocking cones

When an ion is incident on a surface, the repulsive interaction between the ion and target atom results in the ion being scattered. The total scattering angle is dependent on a number of factors, including the impact parameter, *p*, which corresponds to the distance between the centers of the ion and target atom. The interaction potential creates a region behind the target atom into which no incident ions can penetrate. This region is known as a shadow cone, and is illustrated in figure 3.6. A striking

feature of the shadow cone is that the flux at the very edge of the cone is increased relative to the incident distribution, an effect known as trajectory focussing [1]. This arises from the fact that most ions are forward-scattered through relatively small angles and hence their trajectories tend to accumulate at the edge of the shadow cone. If the edge of the shadow cone is directed on to another atom, as shown in figure 3.6(b), an increase in the backscattered intensity is observed from, in the case shown, the second atomic layer of the sample.

For a screened Coulombic interaction potential, the shadow cone radius, *r*, is given by:

$$r = 2C\sqrt{\frac{Z_1 Z_2 e^2 l}{E}} \tag{3.12}$$

where l is the distance behind the scattering atom, E is the incident ion energy and C is the pre-calculated screening factor [11].

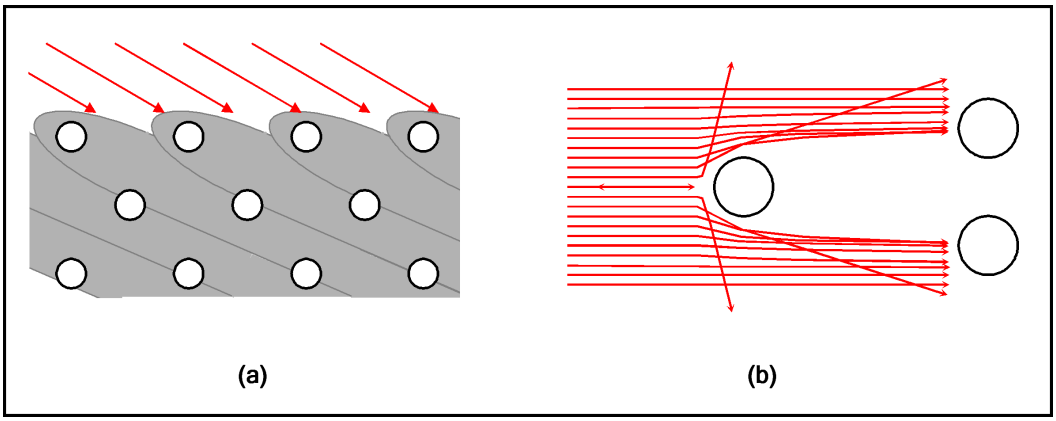

Figure 3.6: Illustration of the creation of a shadow cone behind a surface layer atom. (a) shows a geometry where the shadow cones eliminate any contribution from sub-surface atoms in the backscattered flux (the critical angle). (b) demonstrates the principle of trajectory focussing to increase the backscattered yield.

In practice, the shadow cone radius is more commonly used in surface structure determination due to its relationship with the surface critical angle, α_c. The critical angle is the grazing angle at which the shadow cone from one surface layer atom just masks the next atom in the surface layer, as shown in figure 3.7. Just beyond α_c we expect an increase in the backscattered signal as the increased flux at the edge of the

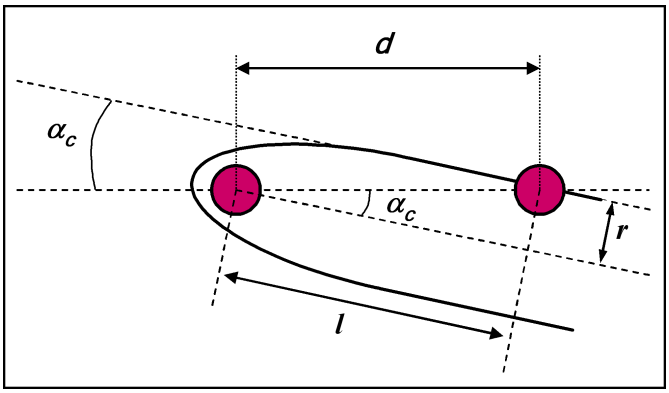

Figure 3.7: Illustration of the shadow cone at the surface critical incidence angle, α_c.

cone is now directly incident on the next atom in the surface layer. Simple geometry relates the shadow cone radius (r) to the distance behind the shadowing atom (l) and the distance between the two atoms (d):

$$r = d \sin \alpha_c \tag{3.13}$$

$$l = d \cos \alpha_c \tag{3.14}$$

The surface critical angle can be obtained from a CAICISS polar angle experiment by measuring the angular position of the first peak in the spectrum. Due to experimental broadening, this is usually measured from the point on the low-angle side of the peak corresponding to 80% - 90% of the maximum intensity. The interatomic spacing can then be calculated using equations 3.12, 3.13 and 3.14. In a similar manner, if the interatomic spacing is well known (e.g. many low-index, clean metal surfaces), α_c can be used to calculate the shadow cone radius. By comparison to the radius arising from an unscreened Coulombic potential [11], the screening factor can be determined. Fauster derived expressions for both the TFM and ZBL models which directly relate the critical angle and interatomic spacing [91]:

$$\begin{aligned} \ln \alpha_c \, (TFM) = 4.6239 + \ln\left(\frac{d}{a}\right)\left(-0.0403 \, \ln\left(\frac{Z_1 Z_2 e^2}{E_0 a}\right) - 0.6730\right) \\ + \ln\left(\frac{Z_1 Z_2 e^2}{E_0 a}\right)\left(-0.0158 \, \ln\left(\frac{Z_1 Z_2 e^2}{E_0 a}\right) + 0.4647\right) \end{aligned} \tag{3.15}$$

$$\ln \alpha_c\,(ZBL) = 4.7334 + \ln\left(\frac{d}{a}\right)\left(- 0.0250\ \ln\left(\frac{Z_1 Z_2 e^2}{E_0 a}\right)\ - 0.7205\right) + \ln\left(\frac{Z_1 Z_2 e^2}{E_0 a}\right)\left(- 0.0094\ \ln\left(\frac{Z_1 Z_2 e^2}{E_0 a}\right)\ +\ 0.3647\right) \tag{3.16}$$

Hence the interatomic spacing on the surface can be estimated relatively straightforwardly from experimental data. Some error is incorporated by the rather arbitrary determination of α_c, but the derived interatomic spacings are generally accurate when compared to studies of the same material system using other techniques.

This argument also holds for particles scattered from the surface, exhibited in the form of blocking cones. With the scattered particles having lower energies, the blocking cones will have slightly larger radii than their shadowing counterparts. Focussing by blocking tends to dominate the backscattered yield at 180° [92], and hence CAICISS is a blocking-dominated technique. As the scattering angle is reduced, a point at which the shadowing and blocking focussing effects are equal is reached at approximately 179°, below which is the domain of ICISS where shadowing dominates. Therefore the annular detector used in CAICISS, capable of detecting particles at a scattering angle of 179°, makes the technique particularly suited to surface structure studies.

3.2.4 Charge exchange, neutralisation and inelastic losses

Since ions are highly unlikely to be in charge equilibrium with the surface, the first processes to occur when an ion is incident on a surface usually involve charge exchange and neutralisation of the ion. Several charge exchange mechanisms exist [1, 5, 81, 87], all of which are fast ($\tau \sim 10^{-14}$ s) when compared to the duration of the scattering event. The processes can result in neutralisation and possibly re-ionisation of the incident ion on both the incoming and outgoing trajectories.

The Auger neutralisation process dominates for noble gas ions and hence is the dominant process in CAICISS [1]. The process is illustrated in figure 3.8. An electron from the surface conduction band tunnels into the potential well of the ion and

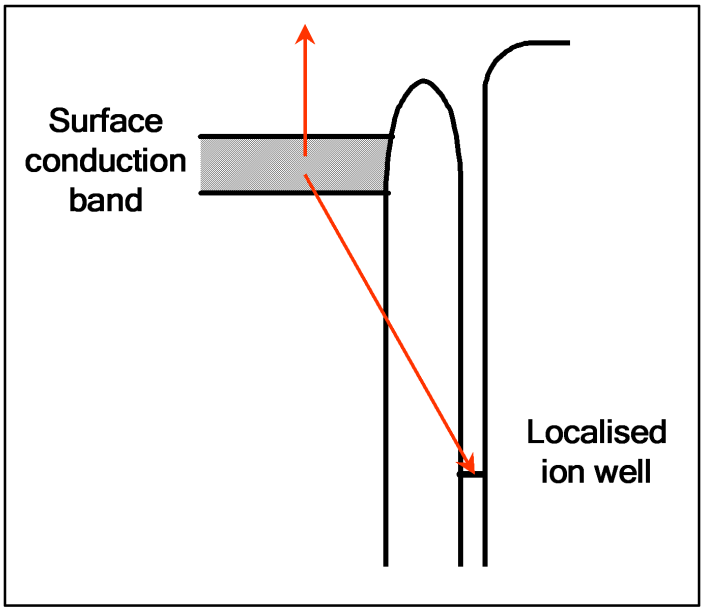

Figure 3.8: Illustration of the Auger neutralisation process. An electron from the surface conduction band tunnels into the potential well of the ion and proceeds to fall down into a deep-lying hole. The electron gives up its excess energy to another surface conduction band electron, which is then emitted from the surface.

proceeds to fall down into a deep-lying hole. The electron gives up its excess energy to another conduction band electron, which is then emitted from the surface. This process leads to the neutralisation of the incident ion.

The low energy (and hence long interaction period) is one reason for the high surface specificity of LEIS experiments, as the probability of neutralisation increases with depth in the sample [1, 87]. Considering this, along with the shadow cones discussed previously, it can be seen that LEIS experiments are ideal for studies of the surface atomic structure. However, to obtain sub-surface structural information, neutral particles scattered from the sample must also be detected as it is very unlikely that particles scattered from sub-surface layers are emitted as ions.

Several other processes can also occur in the collision phase of the interaction, including electronic and nuclear stopping which lead to inelastic energy losses. Electronic stopping arises from the interaction of substrate electrons with the incident ion, causing neutralisation and excitation of the ion. If the ion is then de-excited by

the emission of a photon or electron, the ion loses energy. During nuclear stopping, the incident ion transfers energy and momentum to the substrate atoms. Therefore, any multiple scattered particle reaching the detector is likely to have undergone some degree of energy loss. Further details of two such mechanisms (quasi-single and quasi-double scattering) are given elsewhere [81, 82], but it is believed that such effects are minimised in CAICISS due to the near-180° total scattering angle [93].

3.2.5 Mass resolution

One important issue in CAICISS remains unaddressed. The mass resolution of the experiments has the determining factor on the types of experiments that can be performed using the technique. Several factors, including thermal vibrations, time span of the incident ion pulses, energy spread in the incident beam and the detector resolution can give poor definition of θ and hence limit the mass resolution of a CAICISS scan. However, in the ideal case of a collimated beam, short pulse duration, small angle detector and low thermal vibration, the resolving power ($M_2/\Delta\ M_2$) is dictated by the energy resolving power of the experiment ($E_1/\Delta\ E_1$) [1]. This is given by:

$$\left(\frac{M_2}{\Delta M_2}\right) = \left(\frac{E_1}{\Delta E_1}\right)\left(\frac{2A}{A+1}\right)\left[\frac{A+\sin^2\theta_1-\cos\theta_1(A^2-\sin^2\theta_1)^{1/2}}{A^2-\sin^2\theta_1+\cos\theta_1(A^2-\sin^2\theta_1)^{1/2}}\right] \tag{3.17}$$

and hence for 180° scattering, this expression reduces to:

$$\left(\frac{M_2}{\Delta M_2}\right) = \left(\frac{E_1}{\Delta E_1}\right)\left(\frac{4A}{A^2-1}\right) \tag{3.18}$$

The energy spread of the scattered particles, ΔE_1, is given by:

$$\Delta E_1 = 8\,\frac{A-1}{\left(A+1\right)^2}\,\left(A\ E_0\ E_{phon}\right)^{1/2} \tag{3.19}$$

where E_{phon} is the phonon energy associated with the target atom [5, 94, 95]. Considering typical phonon energies for metals at 300 K, we can see that for 3 keV He^+ incident on Cu, ΔE_1 is of the order of 10 eV and hence $\Delta M_2/M_2 \sim 2.5\%$. Therefore,

elements with a mass differing by at least 10% of the mass of Cu (ie. Fe or lighter, Ge or heavier) can easily be resolved in the ideal case. In practice $\Delta M_2/M_2$ is higher due to factors outlined above, but is sufficiently low for the experiments presented in this thesis. However, it should be noted that the scattering cross-sections of low mass elements (e.g. C, N, O, etc) are too small to yield a signal in the CAICISS spectra given the current setup of the equipment. This will be discussed further in the final chapter of this thesis when modifications to the CAICISS instrument are outlined.

3.3 Low energy electron diffraction (LEED)

Low energy electron diffraction (LEED) is one of the most widely-used tools for the investigation of surface structure [96]. The technique is based on the fact that electrons can be described as wave-like and therefore exhibit characteristics such as diffraction [97, 98]. The electron wavelength is given by the de Broglie relationship:

$$\lambda = (150.4/E)^{1/2} \tag{3.20}$$

Here, λ is the wavelength in Å and E is the electron energy in eV. Therefore, for energies in the region of 10 to 500 eV, the electron wavelength is comparable to typical lattice spacings in crystalline structures and hence diffraction occurs. The diffraction process conserves both energy and momentum, and can be described in terms of electron wavevectors and reciprocal lattice vectors [1]. The Ewald sphere construction, shown in figure 3.9(a), is a three-dimensional representation of the diffraction process in reciprocal space and is used to describe the relationship between the incident electron wavevector **k**, the diffracted wavevector **k'** and the reciprocal lattice vector **g** (**g** = **k'** - **k**). The determination of **g** can then be used to obtain quantitative information on the surface structure via a series of vectorial equations, detailed elsewhere (e.g. [1]).

LEED offers the opportunity to observe diffraction patterns from surfaces since only the component of the wavevector parallel to the surface, $\mathbf{k}_{\|}$, is conserved. The Ewald sphere can easily be adapted to fit this situation, using reciprocal lattice rods perpendicular to the surface, which intercept each point of the reciprocal lattice, as shown in figure 3.9(b). A convenient feature of the 2D Ewald sphere is that all possible

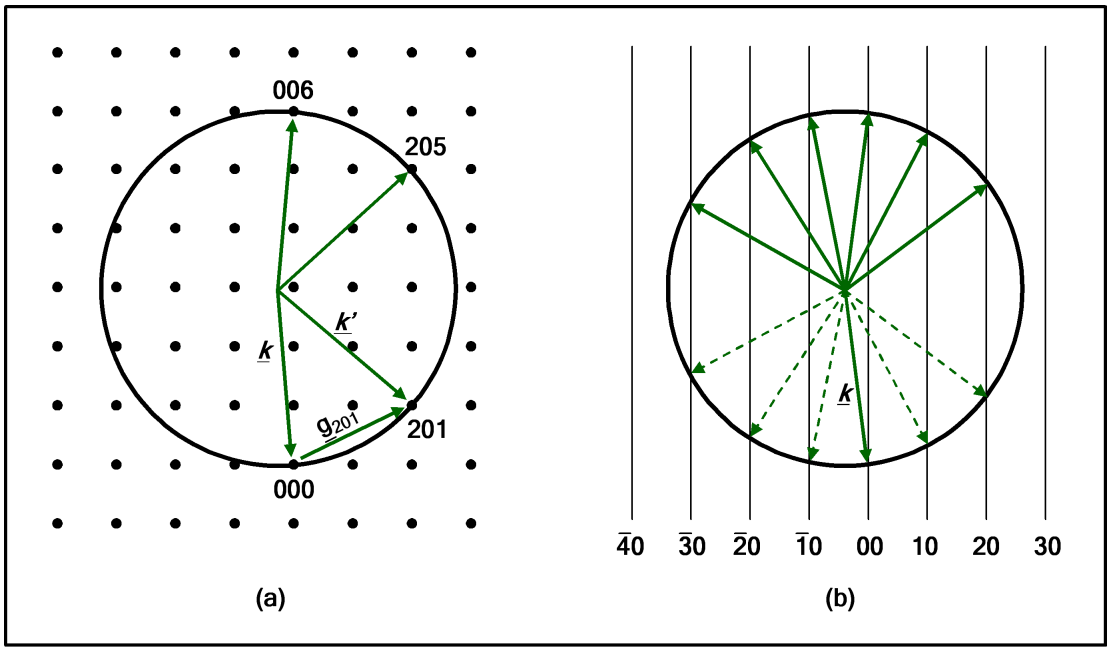

Figure 3.9: (a) The three-dimensional Ewald sphere. For surface techniques such as LEED, this can be adapted to a two-dimensional construction, as shown in (b). In the 2D case, the diffracted beams shown by dashed lines correspond to electrons which are scattered into the bulk of the crystal and cannot be observed. The solid lines represent scattered wavevectors which exit the surface and therefore can be observed in an electron diffraction experiment.

rods within the diameter of the sphere are cut, so a monoenergetic source can be used to observe the entire diffraction pattern. As the energy is increased, the magnitude of $\mathbf{k}_{\parallel}$ increases and more rods are intersected by the sphere, with the lower index beams moving closer together with reference to the radius of the sphere.

The structure and periodicity of a surface can be determined using LEED. The sharpness and background intensity of the pattern acts as a gauge of the quality of the surface, with a high background or diffuse spots indicating some degree of disorder. As LEED shows the periodicity in reciprocal space, features in between the integer order spots are due to real space periodicities which are larger than the (1×1) surface unit mesh. Analysis of such patterns must include the possibility of rotated domains on the surface (e.g. (2×1) and (1×2)), as the observed LEED pattern is simply a combination of the various periodic structures which exist in different regions of the surface.

The surface specificity of LEED arises from the limited penetration depth of low energy electrons ($<$ 100 eV). In most materials this is limited to around 20 Å at low energies [99]. The short mean free path means that electrons cannot escape from deep in the crystal without undergoing one or more inelastic scattering events, making the technique ideal for surface structure determination [1, 5, 96].

A schematic of the retractable Omicron GmbH SpectraLEED system used in this project is shown in figure 3.10. The electron gun contains a LaB_6 filament and produces electrons with an energy spread of $\sim$ 0.5 eV, which are then focussed on to the surface. Backscattered electrons travel from the sample to a set of three spherical grids, via a field-free region (ensured by the first grid being earthed). The second and third grids are set at a potential just below that of the filament to filter out any inelastically scattered electrons. The remaining electrons are then accelerated by a high positive voltage ($\sim$ 5 kV) on to a fluorescent screen. This ensures a visible projection of the surface reciprocal net appears on the screen. The effective magnification of the observed pattern can be adjusted by changing the incident electron energy (and hence changing the radius of the Ewald sphere).

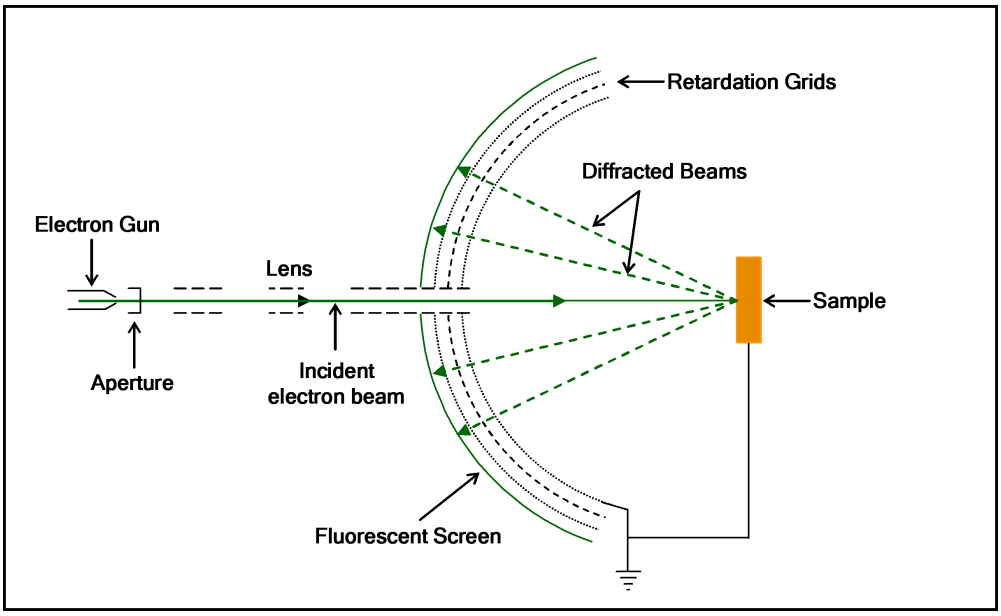

Figure 3.10: Schematic diagram of the LEED apparatus used during this project.

3.4 X-ray photoelectron spectroscopy (XPS)

An overview of the XPS process is shown schematically in figure 3.11. An X-ray photon of energy $h\nu$ penetrates the surface and is absorbed by an electron with binding energy E_b, leading to the emission of the electron from the atom. In the most simple model, the emitted electron would have a kinetic energy, E_k, given by:

$$E_k = h\nu - E_b - \phi \tag{3.21}$$

where ϕ is the work function of the irradiated material. However, when a core hole is created, the surrounding electrons react to the reduced screening potential by relaxing to lower energy states to partially screen the core hole. This gives the outgoing photoelectron an extra energy, E_a, known as the intra-atomic relaxation shift. The generation of a core hole may also lead to an electron from a higher energy level dropping down to fill the hole, causing the emission of a second (Auger) electron with a kinetic energy characteristic of the energy levels involved in the emission. This forms the basis of Auger electron spectroscopy (AES) and is described in detail elsewhere [1, 82]. Alternatively for high mass elements ($Z > 33$), this process can also lead to the emission of an X-ray photon, as detected in X-ray fluorescence (XRF) [1].

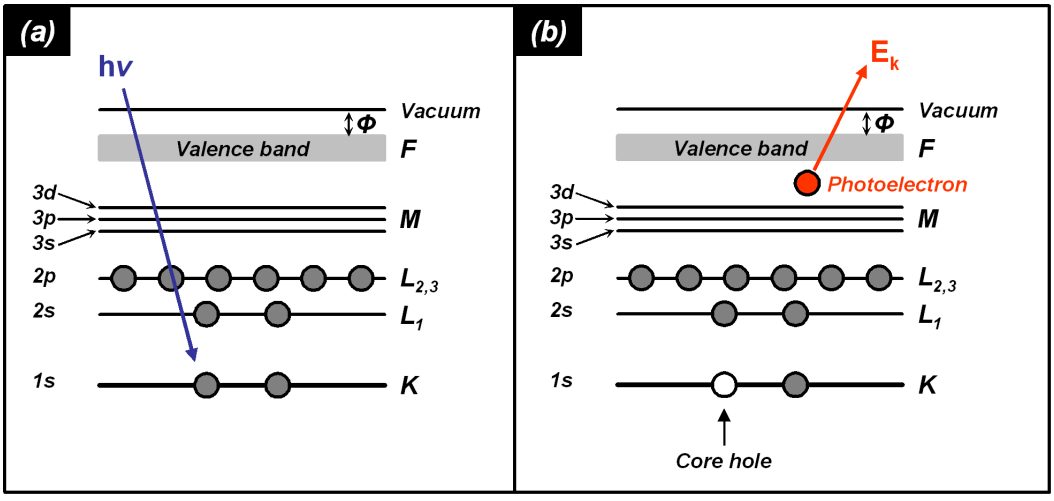

Figure 3.11: Schematic diagram of the physical principles behind XPS. (a) An incident photon with energy $h\nu$ which is absorbed by a core level electron. (b) A photoelectron is emitted with a given kinetic energy, E_k if $h\nu$ is greater than the binding energy of the electron, leaving behind a core hole.

The above description would be adequate for a free atom if photoionisation and photoemission were slow processes and allowed the system to reach a stable equilibrium. In reality, these processes are extremely rapid ($\sim 10^{-14}$ s) and can lead to final state electrons residing in excited bound states, or to the emission of another electron to an unbound state above the vacuum level. Both of these possibilities lead to a reduction in the kinetic energy of the photoelectron. Inelastic scattering of photoelectrons during their escape from the solid results in a loss of kinetic energy and contributes to the background of the XPS spectrum.

For a solid surface, the picture is again modified. In metals, weakly bound (valence) electrons are particularly mobile and help to screen the core hole. Therefore an extra interatomic relaxation shift, E_r must be incorporated to calculate the photoelectron's kinetic energy, so:

$$E_k = h\nu - E_b + E_a + E_r - \phi \tag{3.22}$$

The surface specificity of XPS comes from the relatively short inelastic scattering mean-free-path of the photoelectrons, Λ. This can be described as the thickness of matter which attenuates an incident electron flux, I_0, by a factor of e (see figure 3.12). The detected electron flux at a take-off angle (TOA), θ, after passing through a material of thickness d, in which their inelastic mean-free-path is Λ, without undergoing an inelastic scattering event is given by:

$$I(E) = I_0(E)e^{-d/\Lambda \sin\theta} \tag{3.23}$$

As shown in figure 3.13, $\sim$ 90% of the emitted flux comes from the outermost 2Λ of the material at a TOA of 90°, although the incident X-rays penetrate several μm into the sample. With typical Λ values being around 30 Å, this limits the XPS probing depth to around 100 Å [100]. Figure 3.13 also shows that as the TOA is decreased, the emitted flux becomes more surface specific, with 90% of the detected signal originating from the outermost $\Lambda/2$ at a 15° TOA. With each atomic species having a unique electronic structure, XPS allows highly surface specific studies (at glancing θ values), and overlayer thicknesses can be determined by comparing the intensity at a given θ from the substrate material prior to and following deposition.

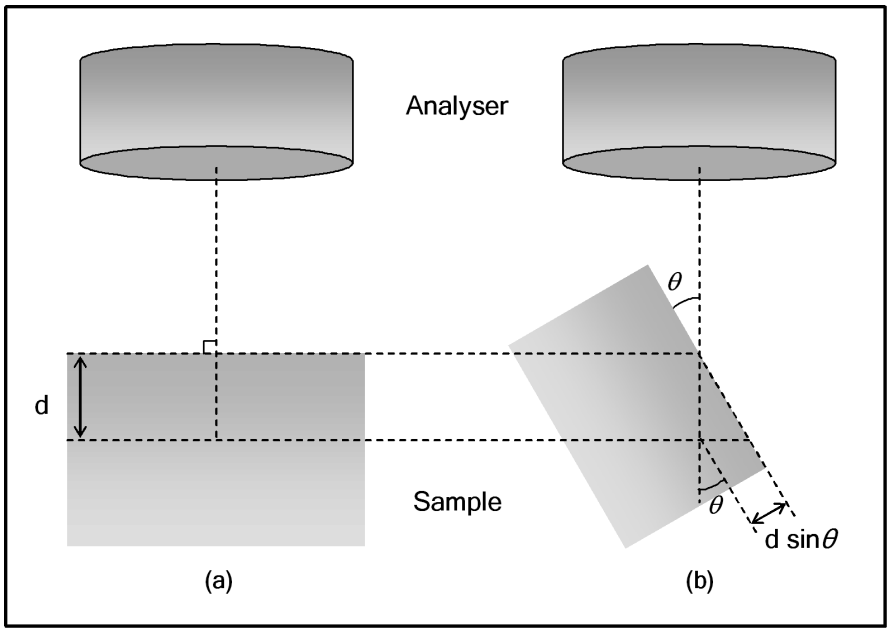

Figure 3.12: A demonstration of the effects of varying the TOA in XPS. (a) shows detection of photoelectrons normal to the surface. By rotating the sample to glancing angles, as in (b), the escape depth, *d*, is reduced, and hence the XPS spectra are more surface specific.

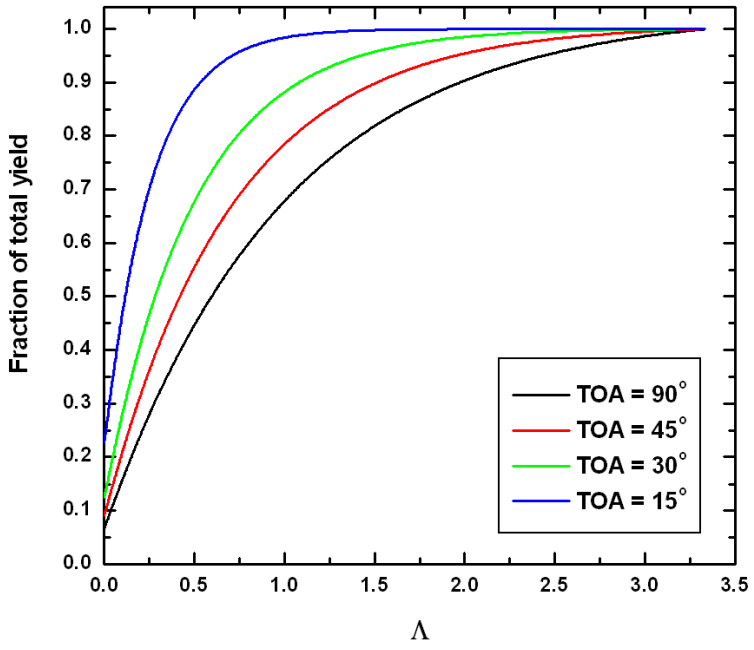

Figure 3.13: The contribution to the XPS spectrum as a function of depth for take-off angles of (a) 90°, (b) 45°, (c) 30° and (d) 15°. The figure illustrates that 90% of the acquired signal originates from the outermost $\sim 2\Lambda$ at a TOA of 90°, reducing to $\sim \Lambda/2$ at 15°.

The surface concentration of an adsorbate, σ, is proportional to the intensity of its photoelectron peaks. Madey *et al.* [101] quantified this by relating the intensity of the peak to the intensity of the photoelectron peak arising from the clean substrate surface. The intensity of the adsorbate photoelectron peak (I_a) and the intensity of the substrate peak (I_s) are related by:

$$\frac{I_a}{I_s} = \frac{\mu'_a M_s \sigma}{N \mu'_s \rho_s \Lambda_s \cos\phi} \tag{3.24}$$

where M_s is the atomic mass of the substrate atoms, σ is the surface concentration of the adsorbate, N is Avagadro's number and ρ_s is the density of the substrate. Λ_s is the mean free path of the photoelectrons in the substrate material and is given by:

$$\Lambda_s = \frac{E_k}{a_s(\ln E_k + b_s)} \tag{3.25}$$

Here, a_s and b_s are functions of the electron concentration as calculated by Penn [100], whilst E_k is the kinetic energy of the photoelectron peak from the substrate. Carley and Roberts [102] modified this description to make use of a modified photoionisation cross-section. Referring back to equation 3.24, μ'_a and μ'_s are the modified photoionisation cross-sections of the adsorbate and substrate respectively, where μ' is given by:

$$\mu' = \mu\left[1 - \frac{\beta}{2}\left(\frac{3\cos^2\phi - 1}{2}\right)\right] \tag{3.26}$$

Values for β have been calculated by Reilman *et al* [103], whilst μ is the unmodified photoionisation cross-section value for the given element, as listed by Scofield [104].

For the purpose of this thesis, XPS has been used to monitor the cleanliness of the surfaces under investigation by monitoring photoemission peaks due to C and O atoms which may have been adsorbed on the surface. The technique has also been used to determine the chemical nature of O atoms adsorbed on the Pt(111) and Ni(110) surfaces, as well as to estimate the coverages of Pt adsorbed on the Cu(100) and Ni(110) surfaces.